Preprints (www.preprints.org) | NOT PEER-REVIEWED | Posted: 29 April 2021 doi:10.20944/preprints202104.0768.v1

Article

Intrinsic dynamic and static nature of halogen bonding in neutral polybromine clusters with the structural feature, elucidated by QTAIM dual functional analysis and MO calculations

Satoko Hayashi *, Taro Nishide, Eiichiro Tanaka and Waro Nakanishi *

[1] Faculty of Systems Engineering, Wakayama University, 930 Sakaedani, Wakayama 640-8510, Japan; hayashi3@sys.wakayama-u.ac.jp and nakanisi@sys.wakayama-u.ac.jp.

* Correspondence: nakanisi@sys.wakayama-u.ac.jp; Tel.: +81-73-457-8252

Abstract: The intrinsic dynamic and static nature of the non-covalent Br-∗-Br interactions in the neutral polybromine clusters is elucidated for Br_4–Br_{12}, applying QTAIM dual functional analysis (QTAIM-DFA). The asterisk (∗) emphasizes the existence of the bond critical point (BCP) on the interaction in question. Data from the fully optimized structures correspond to the static nature of interactions. The intrinsic dynamic nature is originated from those of the perturbed structures generated using the coordinates derived from the compliance constants for the interactions and the fully optimized structures. The non-covalent Br-∗-Br interactions in the L-shaped clusters of the C_s symmetry are predicted to have the typical hydrogen bond nature without covalency, although the first ones in the sequences have the vdW nature. The L-shaped clusters are stabilized by the n(Br)→σ*(Br–Br) interactions. The compliance constants for the corresponding non-covalent interactions are strongly correlated to the E(2) values based on NBO. Indeed, the MO energies seem not contribute to stabilize Br_4 (C_{2h}) and Br_4 (D_{2d}), but the core potentials stabilize them, relative to the case of $2Br_2$, maybe due to the reduced nuclear-electron distances in the average for the dimmers.

Keywords: ab initio calculations; quantum theory of atoms-in-molecules (QTAIM); bromide; structures.

1. Introduction

Halogen bonding is of current and continuous interest [1,2]. A lot of information has been accumulated relevant to the halogen bonding so far [3]. The halogen bonding is discussed on the basis of the shorter distances between halogen and other atoms in crystals [4–6]. The short halogen contacts are found in two types, the symmetric (type **I**) and bent (type **II**) geometries. The bonding is investigated also in the liquid [7,8] and gas [9] phases. The nature of the halogen bonding has been discussed based on the theoretical background, containing the molecular orbital description for the bonding and the σ-hole developed on the halogen atoms, together with the stability with the structural aspects [10]. We also reported the dynamic and static nature of the Y–X---π(C_6H_6) interactions, recently [11]. Halogen bonding is applied to wide variety of field in chemical and biological sciences, such as crystal engineering, supramolecular soft matters and nanoparticles. Efforts have made to unify and categorize the accumulated results and to establish the concept of the halogen bonding [3,12–15].

Structures of halogen molecules (X_2) were reported, determined by the X-ray crystallographic analysis for X = Cl, Br and I [16–18]. The behavior of the bromine–bromine interactions were reported for the optimized structures of Br_2–Br_5 in the neutral and/or charged forms, together with Br_1, so far [19,20]. Figure 1 draws the observed structure of Br_2, for example. The bromine molecules seem to exist as the zig-zag structure in the infinite chains in crystals. One would find the linear alignment of three Br atoms in a L-shaped dimer ((Br_2)$_2$; Br_4) and the linear alignment of four Br atoms in a double

Preprints (www.preprints.org) | NOT PEER-REVIEWED | Posted: 29 April 2021 doi:10.20944/preprints202104.0768.v1

L-shaped trimmer ($(Br_2)_3$; Br_6) in a planar Br_2 layer, in addition to Br_2 itself. The linear four Br atoms are located in the two L-shaped dimers of Br_6, overlapped at the central Br_2. While the L-shaped dimers seem to construct the zig-zag type infinite chains, the linear four Br atoms do the linear infinite chains. The attractive $n_p(Br)\rightarrow\sigma^*(Br–Br)$ σ(3c–4e) (three center–four electron interaction of the σ-type) and $n_p(Br)\rightarrow\sigma^*(Br–Br)\leftarrow n_p(Br)$ σ(4c–6e) must play a very important role to stabilize the Br_4 and Br_6, respectively, where $n_p(Br)$ stands for the p-type non-bonding orbital of Br in the plane, perpendicular to the molecular Br_2 axis, and σ*(Br–Br) is the σ*-orbital of Br_2. The crystal structures of Cl_2 and I_2 are very similar to that of Br_2.

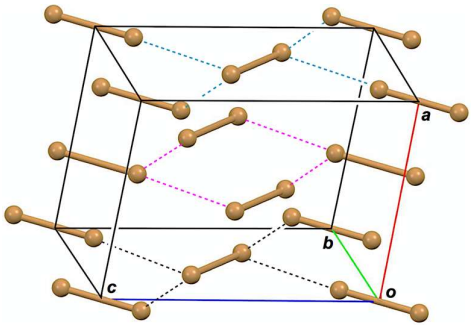

Figure 1. Structure of Br_2, determined by the X-ray crystallographic analysis [17].

We have been much interested in the behavior of the halogen bonding in the polyhalogen clusters, together with the structures. How can the interactions in the polyhalogen clusters be clarified? We proposed QTAIM dual functional analysis (QTAIM-DFA) [21–25], based on the quantum theory of atoms in molecules (QTAIM) approach introduced by Bader [26,27]. In QTAIM-DFA, $H_b(\boldsymbol{r}_c)$ are plotted versus $H_b(\boldsymbol{r}_c) - V_b(\boldsymbol{r}_c)/2$ (= $(\hbar^2/8m)\nabla^2\rho_b(\boldsymbol{r}_c)$; see Equation (SA2) in the Supplementary Materials), where $\rho_b(\boldsymbol{r}_c)$, $H_b(\boldsymbol{r}_c)$, and $V_b(\boldsymbol{r}_c)$ stand for the charge densities, the total electron energy densities, and potential energy densities, respectively, at a bond critical points (BCPs, *) on the bond paths (BPs) in this paper [26]. The kinetic energy densities at BCPs will be similarly denoted by $G_b(\boldsymbol{r}_c)$ [26]. In our treatment, data from the fully optimized structures are plotted, together with those from the perturbed structures around the fully optimized ones. The static nature of the interactions corresponds to the data from the fully optimized structures, which are analyzed using the polar coordinate (R, θ) representation [21–25]. On the other hand, the dynamic nature originates based on the data from both the perturbed and fully optimized structures [21–25]. The plot is expressed by (θ_p, κ_p), where θ_p corresponds to the tangent line and κ_p is the curvature of the plot. θ and θ_p are measured from the y-axis and the y-direction, respectively. We call (R, θ) and (θ_p, κ_p) the QTAIM-DFA parameters. (See also Figure 5 for the definition of (R, θ) and (θ_p, κ_p), illustrated exemplified by the r_9 in Br_{10} (C_s-L_5).)

The perturbed structures necessary for QTAIM-DFA can be generated variously. Among them, a method, employing the coordinates corresponding to the compliance constants C_{ii} for the internal vibrations, is shown to be highly reliable to generate the perturbed structures. The method, which we proposed recently, is called CIV [28–33]. The dynamic nature of interactions based on the perturbed structures with CIV is described as the "intrinsic dynamic nature of interactions" since the coordinates are invariant to the choice of coordinate system. Rough criteria that distinguish the interaction in question from others are obtained by applying QTAIM-DFA with CIV to standard interactions. QTAIM-DFA and the criteria are explained in the Appendix of the Supplementary Materials using Schemes SA1–SA3, Figures SA1 and SA2, Table SA1, and Equations (SA1)–(SA7). The basic concept of the QTAIM approach is also explained.

QTAIM-DFA using the perturbed structures generated with CIV is well-suited to elucidate the intrinsic dynamic and static nature of the halogen-halogen interactions in the polyhalogen clusters. As the first step to clarify the nature of various types of the halogen-halogen interactions in the polyhalogen clusters, the nature of each bromine-bromine interaction in the neutral polybromine clusters is elucidated by applying QTAIM-DFA. Various types of the structures and the interactions

Preprints (www.preprints.org) | NOT PEER-REVIEWED | Posted: 29 April 2021 doi:10.20944/preprints202104.0768.v1

are found in the optimized structures of polybromine clusters, other than those observed in the crystals. Here, we present the results of investigations on the polybromine clusters, together with the structural feature, elucidated with QTAIM-DFA and QC calculations.

2. Methodological details in calculations

Structures were optimized employing the Gaussian 09 programs [34]. The 6-311+G(3df) basis [35–38] set was applied to optimize the structures of neutral polybromine clusters, Br_2–Br_{12}. The Møller-Plesset second order energy correlation (MP2) level [39–41] was applied for the optimizations. Optimized structures were confirmed by the frequency analysis. The results of the frequency analyses were employed to calculate the C_{ij} values and coordinates corresponding to C_{ii} [28,30]. QTAIM functions were calculated using the Gaussian 09 program package [34] with the same method to the optimizations. Data were analyzed with the AIM2000 [42] and AIMAll [43] programs.

Coordinates corresponding to the compliance constants for an internal coordinate i of the internal vibrations ($\mathbf{C}_i$) were employed to generate the perturbed structures, necessary in QTAIM-DFA [21–25]. Equation (1) explains the method to generate the perturbed structures with CIV. A i-th perturbed structure in question ($\mathbf{S}_{iw}$) was generated by the addition of the coordinates ($\mathbf{C}_i$) corresponding to C_{ii} to the standard orientation of a fully-optimized structure ($\mathbf{S}_o$), in the matrix representation. The coefficient g_{iw} in Equation (1) controls the difference in structures between $\mathbf{S}_{iw}$ and $\mathbf{S}_o$: g_{iw} are determined to satisfy Equation (2) for an interaction in question, where r and r_o show the distances in question in the perturbed and fully optimized structures, respectively, with a_o of Bohr radius (0.52918 Å) [21–25,28].

$$\mathbf{S}_{iw} = \mathbf{S}_o + g_{iw} \bullet \mathbf{C}_i \quad (1)$$

$$r = r_o + wa_o \quad (w = (0), \pm0.05 \text{ and } \pm0.1;\ a_o = 0.52918 \text{ Å}) \quad (2)$$

$$y = c_o + c_1x + c_2x^2 + c_3x^3 \quad (R_c^2\text{: square of correlation coefficient}) \quad (3)$$

In the QTAIM-DFA treatment, $H_b(\boldsymbol{r}_c)$ are plotted versus $H_b(\boldsymbol{r}_c) - V_b(\boldsymbol{r}_c)/2$ for data of five points of w = 0, ±0.05 and ±0.1 in Equation (2). Each plot is analyzed using a regression curve of the cubic function as shown in Equation (3), where $(x, y) = (H_b(\boldsymbol{r}_c) - V_b(\boldsymbol{r}_c)/2, H_b(\boldsymbol{r}_c))$ (R_c^2 (square of correlation coefficient) > 0.99999 in usual) [25].

3. Results and Discussion

3.1. Structural optimizations of polybromine clusters, Br_6–Br_{12}

Structures of the neutral Br_2–Br_{12} clusters were optimized with MP2/6-311+G(3df). The structural parameters for the optimized structures of minima for Br_2–Br_6 and Br_8–Br_{12} are collected in Tables S1 and S2, respectively, of the Supplementary Materials. Table 2 contains some transition states (TSs) for Br_4 and Br_6. The notation of C_s-L_m (m = 1–5) is used for the linear L-shaped clusters of the C_s symmetry, where m stands for the number of the non-covalent interactions in Br_{2m+2} (m = 1–5). Cyclic structures are also optimized retaining the higher symmetries. The optimized structures are not shown in figures but they can be found in the molecular graphs with the contour maps of $\rho(\boldsymbol{r})$, drawn on the optimized structures with MP2/6-311+G(3df). (See Figure 3 for Br_6–Br_{12} of the L-shaped clusters in the C_s symmetry, Br_6 (C_s-L_2)–Br_{12} (C_s-L_5) with Br_4 (C_s-L_2) and Figure 4 for Br_4–Br_{12} of minima other than C_s-L_m (m = 1–5)). The energies for the formation of Br_4–Br_6 and Br_8–Br_{12}, are given in Tables S1 and S2 of the Supplementary Materials, respectively, from the components ($\Delta E = E(Br_{2k}) - kE(Br_2)$) on the energy surfaces (ΔE_{ES}) and those with the collections of the zero-point energies (ΔE_{ZP}). The ΔE_{ZP} values were plotted versus ΔE_{ES}. The plot is shown in Figure S1 of the Supplementary Materials, which gives an excellent correlation ($y = 0.940x + 0.129$; R_c^2 (square of correlation coefficient) = 0.9999, see also entry 1 in Table 3). Therefore, the ΔE_{ES} values are employed for the discussion.

The behavior of the neutral di-bromine clusters (Br_4) is discussed, first. Three structures were optimized for Br_4, as minima with some TSs. The minima are the L-shaped structure of the C_s

Preprints (www.preprints.org) | NOT PEER-REVIEWED | Posted: 29 April 2021 doi:10.20944/preprints202104.0768.v1

symmetry (Br_4 (C_s-L_1)) [19], cyclic structure of the C_{2h} symmetry (Br_4 (C_{2h})), and the tetrahedral type of the D_{2d} symmetry (Br_4 (D_{2d})). A TS of the C_s symmetry was detected between Br_4 (C_s-L_1) and Br_4 (C_{2h}) and two TSs of the C_1 symmetry were between Br_4 (C_{2h}) and Br_4 (D_{2d}) and between Br_4 (D_{2d}) and Br_4 (C_s-L_1). They are called TS (C_s: C_s, C_{2h}), TS (C_1: C_{2h}, D_{2d}), and TS (C_1: D_{2d}, C_s), respectively. The three minima will be converted to each other through the tree TSs. A TS between Br_4 (C_s-L_1) and its topological isomer was also detected, which is called TS (C_{2v}: C_s, C_s), however, further effort was not made to search similar TSs between Br_4 (C_{2h}) and its topological isomer and between Br_4 (C_{2d}) and the topological isomer.

Figure 2 draws the energy profiles for the optimized structures of minima, Br_4 (C_s-L_1), Br_4 (C_{2h}), and Br_4 (D_{2d}), together with the TSs, TS (C_s: C_s, C_{2h}), TS (C_s: C_{2h}, D_{2d}), TS (C_1: C_{2d}, C_s) and TS (C_{2v}: C_s, C_s). The optimized structures are not shown in figures but they can be found in the molecular graphs shown in Figure 2, illustrated on the optimized structures. All BCPs expected are detected clearly, together with RCPs and a CCP [26]. The ΔE_{ES} value of –10.7 kJ mol^{-1} for the formation of Br_4 (C_s-L_1) seems very close to the border area between the vdW and typical hydrogen bond (*t*-HB) adducts. The driving force for the formation of Br_4 (C_s-L_1) must be Br_3 σ(3c–4e) of the n_P(Br)→σ*(Br–Br) type. The interactions in Br_4 (C_{2h}) and Br_4 (D_{2d}) seem very different from that in Br_4 (C_s-L_1). The ΔE_{ES} values of Br_4 (C_{2h}) (–8.0 kJ mol^{-1}) and Br_4 (D_{2d}) (–9.1 kJ mol^{-1}) are close to that for Br_4 (C_s-L_1) (–10.7 kJ mol^{-1}). Moreover, the values for TS (C_s: C_s, C_{2h}) (–7.4 kJ mol^{-1}), TS (C_1: C_{2h}, D_{2d}) (–7.6 kJ mol^{-1}), TS (C_1: D_{2d}, C_s) (–7.0 kJ mol^{-1}), and TS (C_{2v}: C_s, C_s) (–8.7 kJ mol^{-1}) are not so different from those for the minima.

In the case of Br_6, three structures of the linear C_s-symmetry (Br_6 (C_s-L_2)), the linear C_2-symmetry (Br_6 (C_2)) and the cyclic C_{3h} symmetry (Br_6 (C_{3h}-*c*)) were optimized typically as minima. The linear Br_6 clusters of the C_{2h}-symmetry (Br_6 (C_{2h})) and the C_{2v}-symmetry (Br_6 (C_{2v})), similar to Br_6 (C_2), were also optimized, of which the torsional angles, ϕ(^{1}Br^{2}Br^{5}Br^{6}Br) (= ϕ_3), were 0° and 180°, respectively. One imaginary frequency was detected for each, therefore, they are assigned to TSs between Br_6 (C_2) and the topological isomer on the different reaction coordinates. Further effort was not made to search TSs.

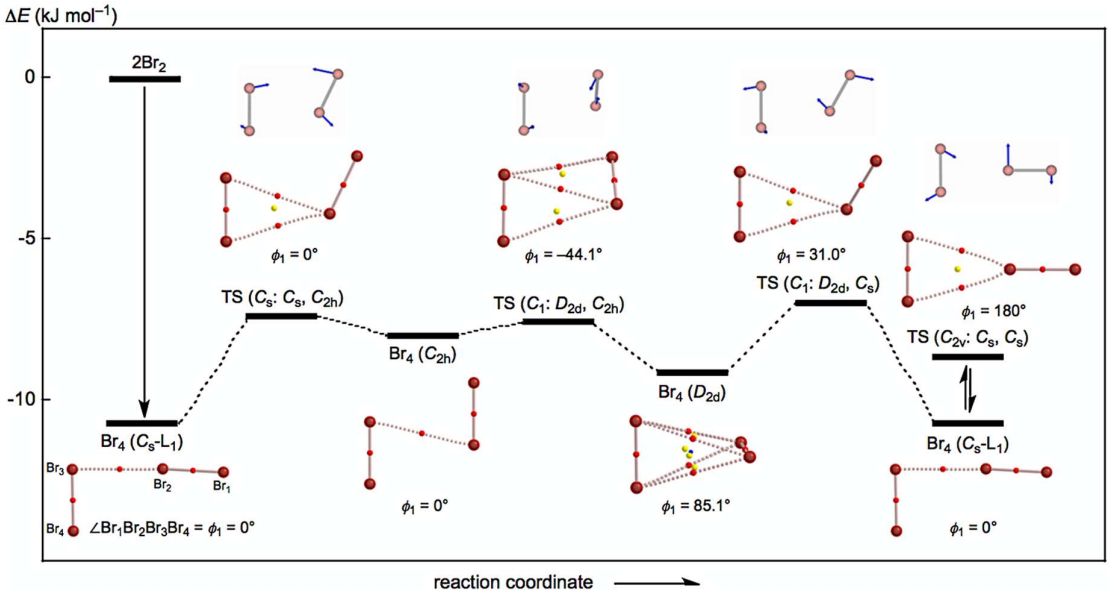

Figure 2. Energy profile with molecular graphs for the structures of Br_4 clusters, optimized with MP2/6-311+G(3df).

The ΔE_{ES} value for Br_6 (C_s-L_2) was predicted to be –22.6 kJ mol^{-1}. The magnitude is slightly larger than the twice value for Br_4 (C_s-L_1) (ΔE_{ES} = –10.7 kJ mol^{-1}). Two types of σ(3c–4e) operate to stabilize Br_6 (C_s-L_2). One σ(3c–4e) seems similar to that in Br_4 (C_s-L_1) but another would be somewhat different. Namely, the second interaction would contribute to ΔE_{ES} somewhat larger than that of the first one in the formation of Br_6 (C_s-L_2). On the other hand, the linear interaction in Br_6 (C_2) can be explained

Preprints (www.preprints.org) | NOT PEER-REVIEWED | Posted: 29 April 2021 doi:10.20944/preprints202104.0768.v1

by σ(4c–6e) of the n_P(Br)→σ*(Br–Br)←n_P(Br) type. The magnitude of ΔE_{ES} of Br_6 (C_2) seems slightly smaller than that of Br_6 (C_s-L_2), but is very close to the twice value for Br_4 (C_s-L_1). The magnitude of ΔE_{ES} for Br_6 (C_{3h}-*c*) is close to the triplicate value of Br_4 (C_s-L_1). One finds triply degenerated σ(3c–4e) interactions in Br_6 (C_{3h}-*c*). The similarity in the interactions for Br_4 (C_s-L_1), Br_6 (C_2) and Br_6 (C_{3h}-*c*) will be discussed later, again (*cf*: Tables 1 and 2). The magnitudes of ΔE_{ES} become larger proportionally to the size of the clusters, as shown in Figures S1 and S2 of the Supplementary Materials. The ΔE_{ES} values are plotted versus *k* in Br_{2k} ($2 \le k \le 6$) for the C_s-L_m type. The results are shown in Figure S2 of the Supplementary Materials. Contributions from inner σ(3c–4e) (named r_{in}) to ΔE_{ES} seems slightly larger than those from σ(3c–4e) in the front end and end positions (named r_2 and r_ω, respectively).

After examination of the optimized structures, next extension is to clarify the nature of the Br-∗-Br interactions by applying QTAIM-DFA. The contour plots are discussed, next.

3.2. Molecular graphs with contour plots of polybromine clusters

Figure 3 illustrates the molecular graphs with the contour maps of $\rho(\boldsymbol{r})$ for the linear type of Br_4 (C_s-L_1)–Br_{12} (C_s-L_5), drawn on the structures optimized with MP2/6-311+G(3df). Figure 4 draws the molecular graphs with the contour maps of $\rho(\boldsymbol{r})$ for Br_4–Br_{12}, other than those for Br_4 (C_s-L_1)–Br_{12} (C_s-L_5), calculated with MP2/6-311+G(3df) [44] (see also Figure S3 of the Supplementary Materials). All BCPs expected are detected clearly, together with RCPs and a CCP, containing those for the non-covalent Br-∗-Br interactions, which are located at the (three dimensional) saddle points of $\rho(\boldsymbol{r})$. All BCPs seem to exist inside of the molecular surfaces of the clusters, except for some, such as those on

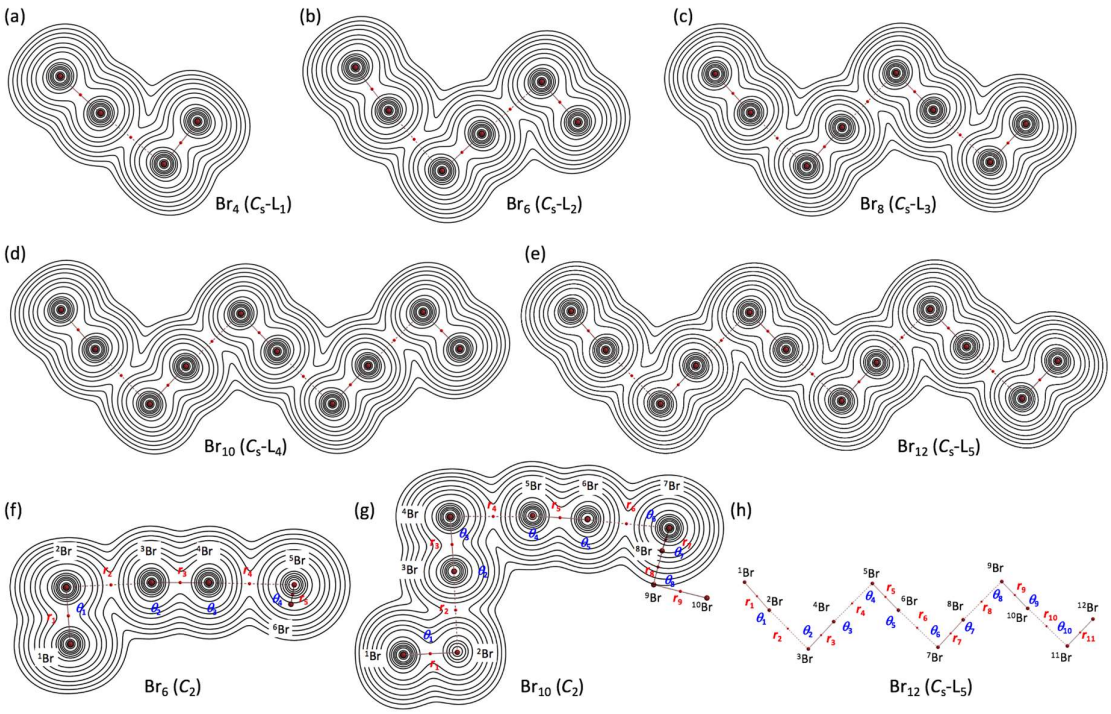

Figure 3. Molecular graphs with contour plots of $\rho(\boldsymbol{r})$ for the linear type bromine clusters of Br_4–Br_{12}, calculated with MP2/6-311+G(3df). (a)–(e) for the linear C_s-L_m type, (f) and (g) for the C_2 type, and (h) for the notations of the atoms, bonds, and angles, exemplified by B_{12} (C_s-L_5). BCPs are denoted by red dots and BPs (bond paths) are by pink lines. Bromine atoms are in reddish brown.

Preprints (www.preprints.org) | NOT PEER-REVIEWED | Posted: 29 April 2021 doi:10.20944/preprints202104.0768.v1

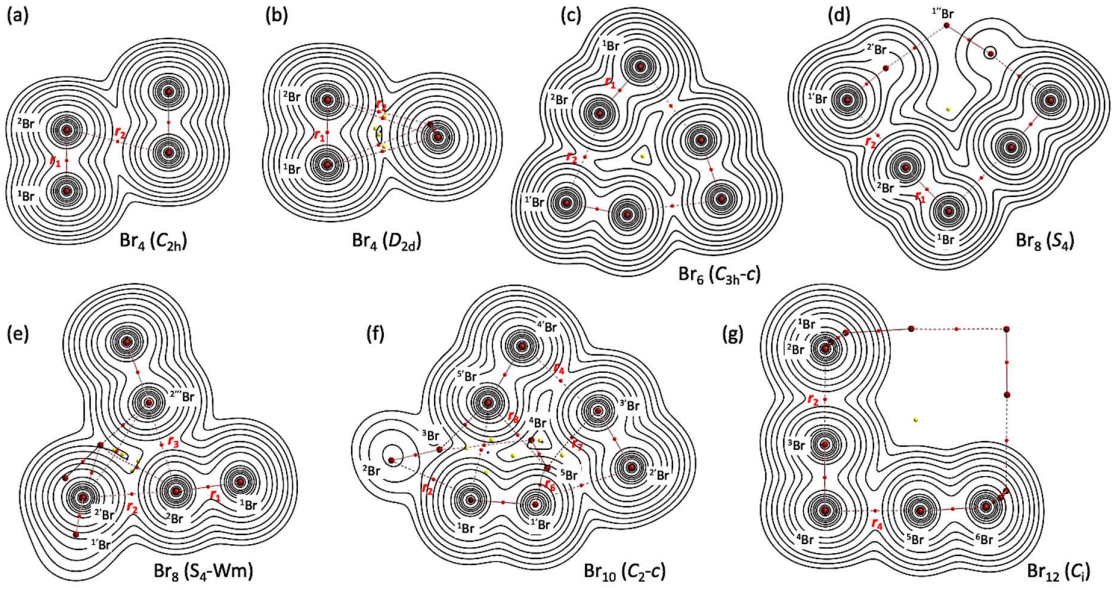

Figure 4. Molecular graphs with contour plots of $\rho(\boldsymbol{r})$ for the cyclic bromine clusters of Br_4–Br_{12}, (a)–(g), calculated with MP2/6-311+G(3df). BCPs are denoted by red dots, RCPs (ring-critical points) by yellow dots, CCPs (cage-critical points) by blue dots, and BPs (bond paths) are by pink lines. See ref. [45] for (a).

the non-covalent interactions of Br_4 (D_{2d}), Br_4 (C_{2h}) and Br_8 (S_4-Wm), although they are very near to the surfaces.

3.3. Survey of the Br--Br interactions in polybromine clusters*

As shown in Figures 2–4, BPs in Br_4–Br_{12} seem almost straight. The linearity is confirmed by comparing the lengths of BPs (r_{BP}) with the corresponding straight-line distances (R_{SL}). The r_{BP} and R_{SL} values are collected in Table S3 of the Supplementary Materials, together with the differences between them, Δr_{BP} (= $r_{BP} - R_{SL}$). The magnitudes of Δr_{BP} are less than 0.01 Å, except for r_2 in Br_4 (C_{2v}) (Δr_{BP} = 0.014 Å), r_3 in Br_8 (S_4-Wm) (0.014 Å) and r_2 in Br_{10} (C_2-*c*) (0.012 Å). Consequently, all BPs in Br_4–Br_{12} can be approximated as the straight lines.

QTAIM functions are calculated for the Br-*-Br interactions at BCPs in the structures of Br_2–Br_{12}, optimized with MP2/6-311+G(3df) [44,45]. Table 1 collects the values for the non-covalent Br-*-Br interactions in Br_4–Br_{12} of the C_s-L_m type. Table 2 summarizes the values for the non-covalent Br-*-Br interactions in Br_4–Br_{12}, other than those of the C_s-L_m type. $H_b(\boldsymbol{r}_c)$ are plotted versus $H_b(\boldsymbol{r}_c) - V_b(\boldsymbol{r}_c)/2$ for the data shown in Tables 1 and 2, together with those from the perturbed structures generated with CIV. Figure 5 shows the plots for the non-covalent Br-*-Br interactions and covalent Br-*-Br bonds, exemplified by Br_{10} (C_s-L_4).

QTAIM-DFA parameters of (R, θ) and (θ_p, κ_p) are obtained by analysing the plots of $H_b(\boldsymbol{r}_c)$ versus $H_b(\boldsymbol{r}_c) - V_b(\boldsymbol{r}_c)/2$, according to Equations (S3)–(S6) of the Supplementary Materials. Table 1 collects the QTAIM-DFA parameters for the non-covalent Br-*-Br interactions of Br_4 (C_s-L_1)–Br_{12} (C_s-L_5), Br_6 (C_2), and Br_{10} (C_2), together with the C_{ii} values. Table 2 collects the (R, θ) and (θ_p, κ_p) values for Br_4–Br_{12} other than those given in Table 1, together with the C_{ii} values. The (R, θ) and (θ_p, κ_p) values for the covalent Br-*-Br bonds in Br_4–Br_{12} are collected in Table S4 of the Supplementary Materials.

3.4. The nature of Br--Br interactions in polybromine clusters*

The nature of the covalent and non-covalent Br-*-Br interactions in Br_2–Br_{12} is discussed on the basis of the (R, θ, θ_p) values, employing the standard values as a reference (see Scheme SA3 of the Supplementary Materials).

Preprints (www.preprints.org) | NOT PEER-REVIEWED | Posted: 29 April 2021 doi:10.20944/preprints202104.0768.v1

Table 1 QTAIM functions and QTAIM-DFA parameters for Br-*-Br at BCPs in Br_4 (C_s-L1)–Br_{12} (C_s-L5), together with Br_{10} (C_2) and Br_2, evaluated with MP2/6-311+G(3df).[1]

Species (Symmetry)	BCP on	$\rho_b(\boldsymbol{r}_c)$ (au)	$c\nabla^2\rho_b(\boldsymbol{r}_c)^2$ (au)	$H_b(\boldsymbol{r}_c)$ (au)	R[3] (au)	θ[4] (°)
Br_4 (C_s-L1)	r_2	0.0109	0.0045	0.0014	0.0048	72.5
Br_6 (C_s-L2)	r_2	0.0113	0.0047	0.0014	0.0049	73.0
Br_6 (C_s-L2)	r_4	0.0119	0.0049	0.0014	0.0051	73.7
Br_8 (C_s-L3)	r_2	0.0114	0.0047	0.0014	0.0049	73.2
Br_8 (C_s-L3)	r_4	0.0124	0.0050	0.0014	0.0052	74.4
Br_8 (C_s-L3)	r_6	0.0120	0.0049	0.0014	0.0051	73.9
Br_{10} (C_s-L4)	r_2	0.0114	0.0047	0.0014	0.0049	73.2
Br_{10} (C_s-L4)	r_4	0.0125	0.0051	0.0014	0.0053	74.6
Br_{10} (C_s-L4)	r_6	0.0125	0.0051	0.0014	0.0053	74.6
Br_{10} (C_s-L4)	r_8	0.0120	0.0049	0.0014	0.0051	73.9
Br_{12} (C_s-L5)	r_2	0.0114	0.0047	0.0014	0.0049	73.2
Br_{12} (C_s-L5)	r_4	0.0126	0.0051	0.0014	0.0053	74.7
Br_{12} (C_s-L5)	r_6	0.0127	0.0051	0.0014	0.0053	74.7
Br_{12} (C_s-L5)	r_8	0.0126	0.0051	0.0014	0.0053	74.7
Br_{12} (C_s-L5)	r_{10}	0.0120	0.0049	0.0014	0.0051	73.9
Br_6 (C_2)	r_2	0.0104	0.0044	0.0014	0.0046	72.1
Br_{10} (C_2)	r_2	0.0118	0.0048	0.0014	0.0050	73.6
Br_{10} (C_2)	r_4	0.0106	0.0044	0.0014	0.0046	72.3

[1] The interactions in minima are shown. [2] $c\nabla^2\rho_b(\boldsymbol{r}_c) = H_b(\boldsymbol{r}_c) - V_b(\boldsymbol{r}_c)/2$ where $c = \hbar^2/8m$. [3] $R = [(H_b(\boldsymbol{r}_c) - V_b(\boldsymbol{r}_c)/2)^2 + H_b(\boldsymbol{r}_c)^2]^{1/2}$. [4] $\theta = 90° - \tan^{-1}[H_b(\boldsymbol{r}_c)/(H_b(\boldsymbol{r}_c) - V_b(\boldsymbol{r}_c)/2)]$.

Table 1. *Cont.*

Species (Symmetry)	C_{ii}[5] (Å mdyn^{-1})	$\theta_{p:CIV}$[6] (°)	$\kappa_{p:CIV}$[7] (au^{-1})	Predicted nature
Br_4 (C_s-L1)	15.311	87.8	121.2	*p*-CS/vdW[8]
Br_6 (C_s-L2)	14.984	89.0	124.9	*p*-CS/vdW[8]
Br_6 (C_s-L2)	14.114	90.6	127.3	*p*-CS/*t*-HB[9]
Br_8 (C_s-L3)	14.826	89.2	125.0	*p*-CS/vdW[8]
Br_8 (C_s-L3)	13.590	92.2	132.0	*p*-CS/*t*-HB[9]
Br_8 (C_s-L3)	14.048	90.9	127.1	*p*-CS/*t*-HB[9]
Br_{10} (C_s-L4)	14.751	89.4	126.2	*p*-CS/vdW[8]
Br_{10} (C_s-L4)	13.445	92.6	133.2	*p*-CS/*t*-HB[9]
Br_{10} (C_s-L4)	13.478	92.6	132.5	*p*-CS/*t*-HB[9]
Br_{10} (C_s-L4)	13.983	91.1	128.4	*p*-CS/*t*-HB[9]
Br_{12} (C_s-L5)	14.719	89.5	126.9	*p*-CS/vdW[8]
Br_{12} (C_s-L5)	13.376	92.7	133.3	*p*-CS/*t*-HB[9]
Br_{12} (C_s-L5)	13.334	93.0	134.3	*p*-CS/*t*-HB[9]
Br_{12} (C_s-L5)	13.393	92.8	132.6	*p*-CS/*t*-HB[9]
Br_{12} (C_s-L5)	13.962	91.1	128.8	*p*-CS/*t*-HB[9]
Br_6 (C_2)	16.025	86.7	119.2	*p*-CS/vdW[8]
Br_{10} (C_2)	14.218	90.2	126.7	*p*-CS/*t*-HB[9]
Br_{10} (C_2)	16.378	87.2	120.0	*p*-CS/vdW[8]

[5] Defined in Equation (R1) in the text. [6] $\theta_p = 90° - \tan^{-1}(dy/dx)$, where $(x, y) = (H_b(\boldsymbol{r}_c) - V_b(\boldsymbol{r}_c)/2, H_b(\boldsymbol{r}_c))$. [7] $\kappa_p = |d^2y/dx^2|/[1 + (dy/dx)^2]^{3/2}$. [8] The *pure* CS interaction of the vdW nature. [9] The *pure* CS interaction of the HB nature without covalency.

Preprints (www.preprints.org) | NOT PEER-REVIEWED | Posted: 29 April 2021 doi:10.20944/preprints202104.0768.v1

Table 2 QTAIM functions and QTAIM-DFA parameters for Br-*-Br at BCPs in Br_4–Br_{12}, other than the C_s-L_m structures, evaluated with MP2/6-311+G(3df).[1]

Species (Symmetry)	BCP on	$\rho_b(r_c)$ (au)	$c\nabla^2\rho_b(r_c)^2$ (au)	$H_b(r_c)$ (au)	R[3] (au)	θ[4] (°)
Br_4 (C_{2h})	r_2	0.0055	0.0022	0.0009	0.0024	67.2
Br_4 (D_{2d})	r_2	0.0042	0.0017	0.0007	0.0018	66.0
Br_6 (C_{3h}-c)	r_2	0.0092	0.0038	0.0013	0.0040	70.7
Br_8 (S_4)	r_2	0.0128	0.0051	0.0014	0.0053	74.8
Br_8 (S_4-Wm)[5]	r_2	0.0136	0.0054	0.0013	0.0056	76.0
Br_8 (S_4-Wm)[5]	r_3	0.0038	0.0015	0.0007	0.0016	66.0
Br_{10} (C_2-c)	r_2	0.0087	0.0035	0.0012	0.0037	70.5
Br_{10} (C_2-c)	r_4	0.0097	0.0040	0.0014	0.0042	71.3
Br_{10} (C_2-c)	r_6	0.0110	0.0044	0.0014	0.0046	73.0
Br_{10} (C_2-c)	r_7	0.0049	0.0019	0.0008	0.0021	66.2
Br_{10} (C_2-c)	r_8	0.0049	0.0018	0.0008	0.0020	66.6
Br_{12} (C_i)	r_2	0.0129	0.0052	0.0014	0.0054	75.0
Br_{12} (C_i)	r_4	0.0129	0.0052	0.0014	0.0054	75.0

[1] The interactions in minima are shown. [2] $c\nabla^2\rho_b(r_c) = H_b(r_c) - V_b(r_c)/2$ where $c = \hbar^2/8m$. [3] $R = [(H_b(r_c) - V_b(r_c)/2)^2 + H_b(r_c)^2]^{1/2}$. [4] $\theta = 90° - \tan^{-1}[H_b(r_c)/(H_b(r_c) - V_b(r_c)/2)]$. [5] Image from windmill.

Table 2. *Cont.*

Species (Symmetry)	C_{ii}[6] (Å mdyn^{-1})	$\theta_{p:CIV}$[7] (°)	$\kappa_{p:CIV}$[8] (au^{-1})	Predicted nature
Br_4 (C_{2h})	24.709	73.6	122.9	p-CS/vdW[9]
Br_4 (D_{2d})	40.402	69.6	136.3	p-CS/vdW[9]
Br_6 (C_{3h}-c)	25.617	83.3	121.7	p-CS/vdW[9]
Br_8 (S_4)	13.201	93.5	139.2	p-CS/t-HB[10]
Br_8 (S_4-Wm)[5]	11.294	95.3	139.0	p-CS/t-HB[10]
Br_8 (S_4-Wm)[5]	52.918	67.5	204.0	p-CS/vdW[9]
Br_{10} (C_2-c)	34.402	81.3	112.7	p-CS/vdW[9]
Br_{10} (C_2-c)	23.971	84.7	122.1	p-CS/vdW[9]
Br_{10} (C_2-c)	20.831	87.6	122.6	p-CS/vdW[9]
Br_{10} (C_2-c)	29.570	71.5	118.9	p-CS/vdW[9]
Br_{10} (C_2-c)	37.855	71.8	120.4	p-CS/vdW[9]
Br_{12} (C_i)	13.483	93.7	137.9	p-CS/t-HB[10]
Br_{12} (C_i)	13.482	93.7	137.3	p-CS/t-HB[10]

[5] Image from windmill. [6] Defined in Equation (R1) in the text. [7] $\theta_p = 90° - \tan^{-1}(dy/dx)$, where $(x, y) = (H_b(r_c) - V_b(r_c)/2, H_b(r_c))$. [8] $\kappa_p = |d^2y/dx^2|/[1 + (dy/dx)^2]^{3/2}$. [9] The *pure* CS interaction of the vdW nature. [10] The *pure* CS interaction of the HB nature without covalency.

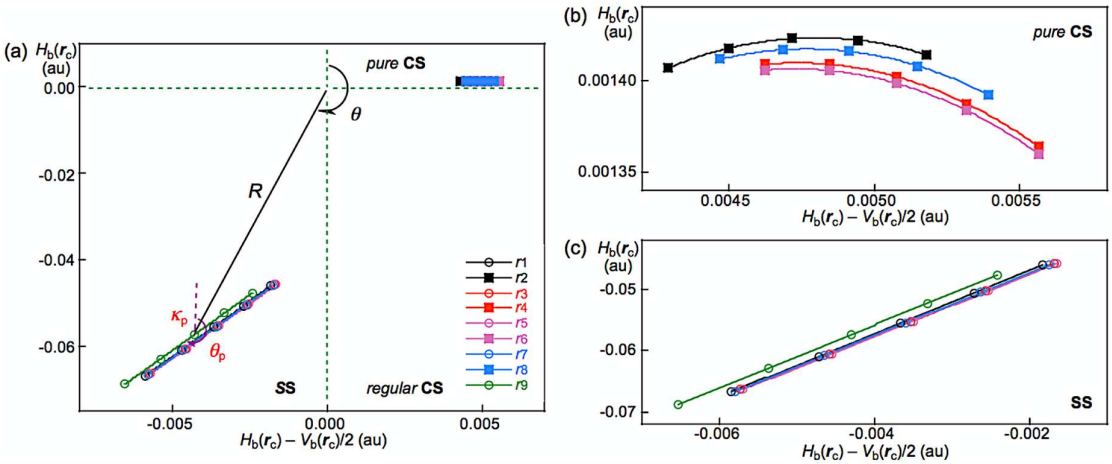

Figure 5. QTAIM-DFA plots ($H_b(r_c)$ versus $H_b(r_c) - V_b(r_c)/2$) for the interactions in Br_{10} (C_s-L_4) evaluated with MP2/6-311+G(3df). Marks and colors are shown in the figure.

Preprints (www.preprints.org) | NOT PEER-REVIEWED | Posted: 29 April 2021 doi:10.20944/preprints202104.0768.v1

It must be instructive to survey the criteria shown in Scheme SA3 of the Supplementary Materials, before detail discussion. The criteria tells us that $180° < \theta$ ($H_b(\boldsymbol{r}_c) - V_b(\boldsymbol{r}_c)/2 < 0$) for the SS interactions and $\theta < 180°$ ($H_b(\boldsymbol{r}_c) - V_b(\boldsymbol{r}_c)/2 > 0$) for the CS interactions. The CS interactions are sub-divided into *pure*-CS interactions (*p*-CS) of $45° < \theta < 90°$ ($H_b(\boldsymbol{r}_c) > 0$) and *regular*-CS interactions (*r*-CS) of $90° < \theta < 180°$ ($H_b(\boldsymbol{r}_c) < 0$). The θ_p value predicts the character of interactions. In the *pure*-CS region of $45° < \theta < 90°$, the character of interactions will be the vdW type for $45° < \theta_p < 90°$ and the *typical*-HB type with no covalency (*t*-HB$_{nc}$) for $90° < \theta_p < 125°$, where $\theta_p = 125°$ approximately corresponds to $\theta = 90°$. The classical chemical covalent bonds of SS ($180° < \theta$) will be strong when $R > 0.15$ au (Cov-s: strong covalent bonds), whereas they will be weak for $R < 0.15$ au (Cov-w: weak covalent bonds).

The (R, θ, θ_p) values are (0.0576 au, 184.3°, 190.9°) for the original Br_2, if evaluated with MP2/6-311+G(3df). Therefore, the nature of the Br-∗-Br bond in Br_2 is classified by the SS interactions ($\theta > 180°$) and characterized to have the Cov-w nature ($\theta_p > 180°$ and $R < 0.15$ au). The nature is denoted by SS/Cov-w. The (R, θ, θ_p) values for the covalent Br-∗-Br bonds in Br_4–Br_{12} are (0.0472–0.0578 au, 182.0–184.4°, 190.4–192.1°), therefore, the nature is predicted to be SS/Cov-w. The nature of the covalent Br-∗-Br bonds seems not changed so much in the formation of the clusters [44]. The non-covalent Br-∗-Br interactions in Br_4–Br_{12} are all classified by the *pure*-CS interactions, since $\theta \leq 76°$ (<< 90°) [44]. The θ_p values in the C_s-L$_m$ clusters change systematically. The θ_p values for r_2 in Br_{2k} (C_s-L$_m$) (k = 2–6) are predicted to be in the range of $89.1° \leq \theta_p \leq 89.6°$ with $\theta_p = 87.9°$ for Br_4 (C_s-L$_1$).

However, the values for r_{n-2} in Br_{2k} (C_s-L$_m$) (k = 2–6) are in the range of $90.6° \leq \theta_p \leq 91.2°$ and the values for the non-covalent interactions other than the edge positions are in the range of $92.1° \leq \theta_p \leq 93.0°$. Namely, the non-covalent Br-∗-Br interactions are predicted to have the vdW nature (*p*-CS/vdW) for r_2. While, the interactions other than r_2 are predicted to have the *t*-HB$_{nc}$ nature (*p*-CS/*t*-HB$_{nc}$), since $\theta_p > 90°$. The θ_p values of r_2 for the C_s-L$_m$ clusters will be less than 90°, irrespective of the angles between r_1 and r_2, which are close to 180°. The θ_p values will be larger than 90° for all non-covalent interactions other than r_2. Table 1 contains the data for Br_{10} (C_2), of which $\theta_p = 90.4°$ (> 90°) for r_2 and $\theta_p = 87.1°$ (< 90°) for r_4, although Br_{10} (C_2) is not the C_s-L$_m$ type. The results for r_2 seem reasonable based on the structure (*cf*: Figure 3), while those for r_4 would be complex. Table 1 summarizes the predicted nature.

In the case of the non-covalent Br-∗-Br interactions in Br_4–Br_{12} other than the C_s-L$_m$ type clusters, $\theta_p > 90°$ for r_2 in Br_8 (S_4) ($\theta_p = 93.4°$) and Br_8 (S_4-Wm) ($\theta_p = 94.8°$) and for r_2, r_4 and r_6 in Br_{12} (C_i) ($93.4° \leq \theta_p \leq 93.7°$). The interactions would have the *t*-HB$_{nc}$ nature (*p*-CS/*t*-HB$_{nc}$). Very weak non-covalent Br-∗-Br interactions are also detected. The ranges of $64.2° \leq \theta \leq 66.6°$ and $66.2° \leq \theta_p \leq 71.2°$ are predicted for r_2 and r_3 in Br_4 (C_{2h}), r_2 in Br_4 (C_{2v}), r_3 in Br_8 (S_4-Wm) and r_7 and r_8 in Br_{10} (C_2-*c*). The results are summarized in Table 2.

What are the relations between the QTAIM-DFA parameters for the non-covalent Br-∗-Br interactions? The θ and θ_p values are plotted versus R. The plots are shown in Figure S4 of the Supplementary Materials. They gave very good correlations. The θ_p values are plotted versus θ. The plot is shown in Figure S5 of the Supplementary Materials. It also gave a very good correlation. Table 3 summarizes the correlations among the QTAIM-DFA parameters.

Table 3. Correlations in the plots.[1]

Entry	Correlation	*a*	*b*	R_c^2	*n*
1	ΔE_{ZP} *vs.* ΔE_{ES}	0.940	0.129	0.9999	20[2]
2	θ *vs.* R	2595.6	60.70	0.979	33
3	θ_p *vs.* R	6449.1	58.19	0.989	33
4	θ_p *vs.* θ	2.67	–106.26	0.992	31[3]
5	$E(2)$ *vs.* C_{ii}^{-1}	535.5	–18.22	0.997	15[4]
6	$E(2)$*vs.* R	9760.9	–29.92	0.983	15[4]
7	$E(2)$ *vs.* θ	2.446	–160.88	0.996	15[4]
8	$E(2)$ *vs.* θ_p	1.067	77.17	0.999	15[4]

[1] The constants (a, b, R_c^2) are the correlation constant, the y-intercept and the square of correlation coefficient, respectively, in $y = ax + b$. [2] Containing TS species. [3] Neglecting the data of r_2 and r_3 in Br_4 (C_{2h}). [4] For the non-covalent Br-∗-Br interactions in Br_4 (C_s-L$_1$)–Br_{12} (C_s-L$_5$).

Preprints (www.preprints.org) | NOT PEER-REVIEWED | Posted: 29 April 2021 doi:10.20944/preprints202104.0768.v1

To examine the behavior of the non-covalent Br-∗-Br interactions, further, NBO analysis is applied to the interactions, next.

3.5. NBO analysis for Br-∗-Br of Br_4 (C_s-L_1)–Br_{12} (C_s-L_5)

The non-covalent Br-∗-Br interactions in Br_4(C_s-L_1)–Br_{12} (C_s-L_5) are characterized by σ(3c–4e) of the n(Br)→σ*(Br–Br) type. NBO analysis [46–48] was applied to the n(Br)→σ*(Br–Br) interactions with MP2/6-311+G(3df). For each donor NBO (i) and acceptor NBO (j), the stabilization energy E(2) is calculated based on the second-order perturbation theory in NBO. The E(2) values are calculated according to in Equation (4), where q_i is the donor orbital occupancy, ε_i, ε_j are diagonal elements (orbital energies) and $F(i,j)$ is the off-diagonal NBO Fock matrix element. The values are obtained separately by the contributions from n_s(Br)→σ*(Br–Br) and n_p(Br)→σ*(Br–Br), which are summarized in Table S5 of the Supplementary Materials. The total values corresponding to n_{s+p}(Br)→σ*(Br–Br) (= n_s(Br)→σ*(Br–Br) + n_p(Br)→σ*(Br–Br)) are calculated, which are also summarized in Table S5 of the Supplementary Materials. The total values are employed for the discussion.

$$E(2) = q_i \times F(i,j)^2/(\varepsilon_j - \varepsilon_i) \quad (4)$$

Figure 6 shows the plots of E(2) and θ_p for the non-covalent Br-∗-Br interactions in Br_4 (C_s-L_1)–Br_{12} (C_s-L_5). The values become larger in the order of P (r_2: Br_4 (C_s-L_1)) < P (r_2: Br_6 (C_s-L_2)–Br_{12} (C_s-L_5)) < P (r_ω: Br_6 (C_s-L_2)–Br_{12} (C_s-L_5)) < P (r_{in}: Br_6 (C_s-L_2)–Br_{12} (C_s-L_5)), where P means E(2) or θ_p, while r_ω and r_{in} stand for the last end and the inside non-covalent interactions, respectively, in the sequence (see, Figures 2 and 3). The values for P = E(2) are as follows: E(2) = 16.6 kJ mol^{-1} for r_2 in Br_4 (C_s-L_1) < 17.7 ≤ E(2) ≤ 18.2 kJ mol^{-1} for r_2 in Br_6 (C_s-L_2)–Br_{12} (C_s-L_5) < 19.5 ≤ E(2) ≤ 20.0 kJ mol^{-1} for r_ω in Br_6 (C_s-L_2)– Br_{12} (C_s-L_5) < 21.2 ≤ E(2) ≤ 22.0 kJ mol^{-1} for r_{in} in Br_8 (C_s-L_3)–Br_{12} (C_s-L_5).

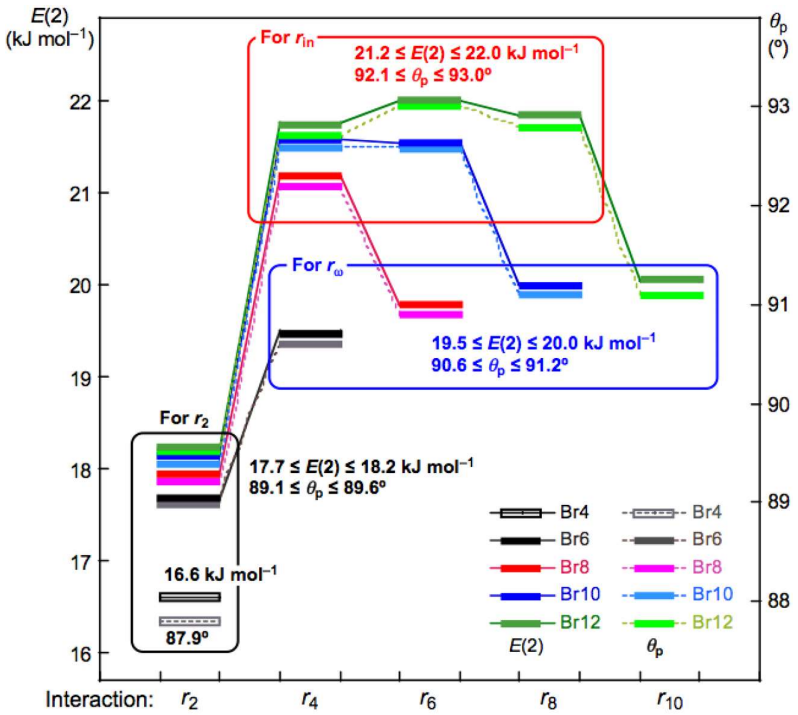

Figure 6. Plots of θ_p and E(2) for the non-covalent Br-∗-Br interactions in Br_4 (C_s-L_1)–Br_{12} (C_s-L_5). Colours are shown in the figure.

Relations between E(2) and C_{ii} were also examined for the non-covalent Br-∗-Br interactions in Br_4 (C_s-L_1)–Br_{12} (C_s-L_5). The E(2) values were plotted versus C_{ii}^{-1} for the non-covalent interactions. Figure 7 shows the plot. The plot gives a very good correlation, which is shown in Table 3 (entry 5).

Preprints (www.preprints.org) | NOT PEER-REVIEWED | Posted: 29 April 2021 doi:10.20944/preprints202104.0768.v1

The results show that the energies for σ(3c–4e) of the n_P(Br)→σ*(Br–Br) type in Br_4 (C_s-L_1)–Br_{12} (C_s-L_5) are well evaluated not only by $E(2)$ but also by C_{ii}^{-1}. Similar relations would be essentially observed for the interactions in the non-linear clusters, however, the analyses will be much complex due to the unsuitable structures for the NBO analysis, such as the deviations in the interaction angles expected for Br_3 σ(3c–4e), the mutual interactions between Br_3 σ(3c–4e), and/or the steric effect from other bonds and interactions, placed proximity in space. The $E(2)$ values for Br_4 (C_s-L_1)–Br_{12} (C_s-L_5) were also plotted versus R, θ, and θ_P, which are shown in Figures S6–S8, respectively, of the Supplementary Materials. The plots gave very good correlations, which are given in Table 3 (entries 6–8).

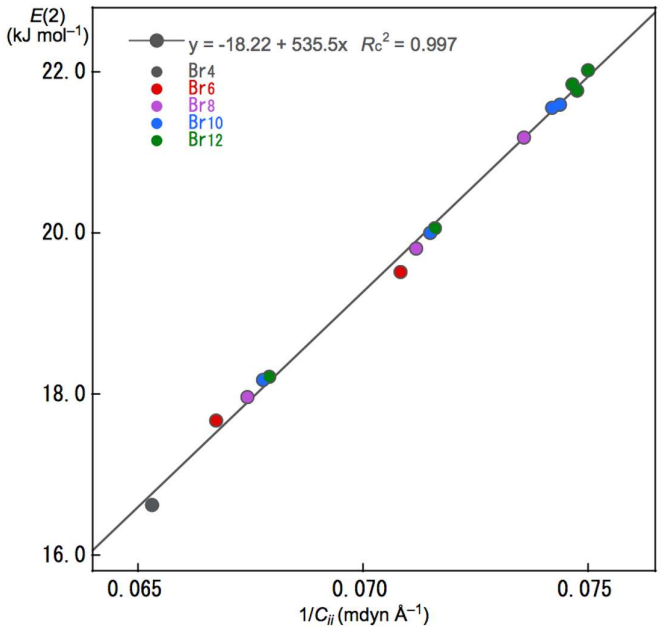

Figure 7. Plot of $E(2)$ versus $1/C_{ii}$ for the non-covalent Br-∗-Br interactions in Br_4 (C_s-L_1)–Br_{12} (C_s-L_5).

3.6. MO descriptions for non-covalent Br-∗-Br interactions in Br_4

As discussed above, Br_3 σ(3c–4e) of the n_P(Br)→σ*(Br–Br) type plays an important role in the formation of Br_4 (C_s-L_1)–Br_{12} (C_s-L_5). However, there must exist some interactions, other than Br_3 σ(3c–4e), to stabilize the clusters. The ΔE_{ES} values for Br_4 (C_{2h}) (–8.0 kJ mol^{-1}) and Br_4 (D_{2d}) (–9.1 kJ mol^{-1}) are not so different from that for Br_4 (C_s-L_1) (–10.7 kJ mol^{-1}). However, Br_4 (C_{2h}) and Br_4 (D_{2d}) must consist of the interactions, other than σ(3c–4e). Indeed, Br_3 σ(3c–4e) of the n(Br)→σ*(Br–Br) type contributes to stabilise Br_4 (C_s-L_1), but Br_4 (C_{2h}) and Br_4 (D_{2d}) are shown to be stabilised by the σ(Br–Br)→σ*Ry(Br) interaction by NBO, where Ry stands for the Rydberg term, although not shown.

The total energy for a species (E) is given by the sum of the core terms ($H_c(i)$) over all electrons, $\Sigma_i^n H_c(i)$ and the electron-electron repulsive terms, $(\Sigma_{i\neq j}^n J_{ij} - \Sigma_{i\neq j,||}^n K_{ij})/2$, as shown by Equation (5), where $H_c(i)$ consists of the kinetic energy and electron-nuclear attractive terms for electron i. E contains the nuclear-nuclear repulsive terms, although not clearly shown in Equation (5). As shown in Equation (6), the sum of MO energy for electron i, ε_i, over all electrons, $\Sigma_{i=1}^n \varepsilon_i$, will be larger than E by $(\Sigma_{i\neq j}^n J_{ij} - \Sigma_{i\neq j,||}^n K_{ij})/2$, since the electron-electron repulsions are doubly counted in Equation (6). Therefore, $\Sigma_i^n H_c(i)$ and $(\Sigma_{i\neq j}^n J_{ij} - \Sigma_{i\neq j,||}^n K_{ij})/2$ are given separately by Equations (7) and (8), respectively. The ε_i values for Br_4 (C_{2h}), Br_4 (D_{2d}) and $2Br_2$, together with Br_4 (C_s-L_1), are collected in Tables S6–S9, respectively, of the Supplementary Materials, for convenience of discussion. Parameters (ΔP) in the formation of Br_{2k} from the components are evaluated according to Equation (9). The $\Delta\Sigma_i^n H_c(i)$ and $\Delta(\Sigma_{i\neq j}^n J_{ij} - \Sigma_{i\neq j,||}^n K_{ij})/2$ values for the formation of Br_4 (C_{2h}), Br_4 (D_{2d}) and Br_4 (C_s-L_1) are collected in Table S11 of the Supplementary Materials.

Preprints (www.preprints.org) | NOT PEER-REVIEWED | Posted: 29 April 2021 doi:10.20944/preprints202104.0768.v1

$$E = \Sigma_i^n H_c(i) + (\Sigma_{i\neq j}^n J_{ij} - \Sigma_{i\neq j,||}^n K_{ij})/2 \quad (5)$$

$$\Sigma_{i=1}^n \varepsilon_i = \Sigma_i^n H_c(i) + (\Sigma_{i\neq j}^n J_{ij} - \Sigma_{i\neq j,||}^n K_{ij}) \quad (6)$$

$$\Sigma_i^n H_c(i) = 2E - \Sigma_{i=1}^n \varepsilon_i \quad (7)$$

$$(\Sigma_{i\neq j}^n J_{ij} - \Sigma_{i\neq j,||}^n K_{ij})/2 = \Sigma_{i=1}^n \varepsilon_i - E \quad (8)$$

$$\Delta P(\mathrm{Br2}_k) = P(\mathrm{Br2}_k) - kP(\mathrm{Br}_2) \quad (9)$$

The nature of the non-covalent Br---Br interactions in Br_4 (C_s-L_1) is examined, first. The σ(3c–4e) character in Br_4 (C_s-L_1) is confirmed by the natural charge evaluated with NPA (Qn), developed in the formation of Br_4 (C_s-L_1). The evaluated Qn values are Br(1: –0.0128|e⁻|)–Br(2: –0.0002|e⁻|)---Br(3: –0.0010|e⁻|)–Br(4: 0.0140|e⁻|), therefore, Qn(Br(4)–Br(3)) and Qn(Br(2)–Br(1)) are +0.013|e⁻| and –0.013|e⁻|, respectively. Each MO in Br_4 (C_s-L_1) is almost localized on Br(4)–Br(3) or Br(2)–Br(1), except for a few cases. MOs in Br_4 (C_s-L_1) must be affected by the local charge. Each MO energy in Br_4 (C_s-L_1) seem higher than the corresponding value of $2Br_2$ by 10–20 kJ mol⁻¹ if the MO is localized on Br(2)–Br(1), lower by 15–25 kJ mol⁻¹ on Br(3)–Br(4) and slightly lower by 0–5 kJ mol⁻¹ if the MO is localized on the whole molecule. We should be careful, since it depends on the phase in MO and the position of the Br atom(s). Typical cases are shown in Figure S9 of the Supplementary Materials. In total, $\Delta\Sigma_{i=1}^n \varepsilon_i$ is evaluated to be –357.2 kJ mol⁻¹ for Br_4 (C_s-L_1). The results show that Br_4 (C_s-L_1) is stabilized in the formation the dimer from the components through the lowering of the MO energies in total, which is consistent with those evaluated with NBO, discussed above.

Figure 8 shows the plots of $\Delta\Sigma_i^n H_c(i)$ and $\Delta(\Sigma_{i\neq j}^n J_{ij} - \Sigma_{i\neq j,||}^n K_{ij})/2$ for Br_4 (C_s-L_1), Br_4 (C_{2h}) and Br_4 (D_{2d}), together with ΔE_{ES} and $\Delta\Sigma_{i=1}^n \varepsilon_i$. In the case of Br_4 (C_s-L_1), $\Delta\Sigma_i^n H_c(i)$ and $\Delta(\Sigma_{i\neq j}^n J_{ij} - \Sigma_{i\neq j,||}^n K_{ij})/2$ are evaluated to be 335.7 and –346.4 kJ mol⁻¹, respectively, which stabilises Br_4 (C_s-L_1) in total. Two Br_2 molecules in Br_4 (C_s-L_1) will supply wider area for electrons without severe disadvantageous steric compression by the L-shaped structure in a plane. The structural feature of Br_4 (C_s-L_1) may reduce (or may not severely increase) the electron-electron repulsive terms, $\Delta((\Sigma_{i\neq j}^n J_{ij} - \Sigma_{i\neq j,||}^n K_{ij})/2)$, relative to the case of $2Br_2$, although $\Delta\Sigma_i^n H_c(i)$ seems to destabilize it. The $\Delta\Sigma_i^n H_c(i) + \Delta(\Sigma_{i\neq j}^n J_{ij} - \Sigma_{i\neq j,||}^n K_{ij})/2$ value is equal to –10.7 kJ mol⁻¹, which corresponds to the stabilization energy of Br_4 (C_s-L_1), relative to $2Br_2$.

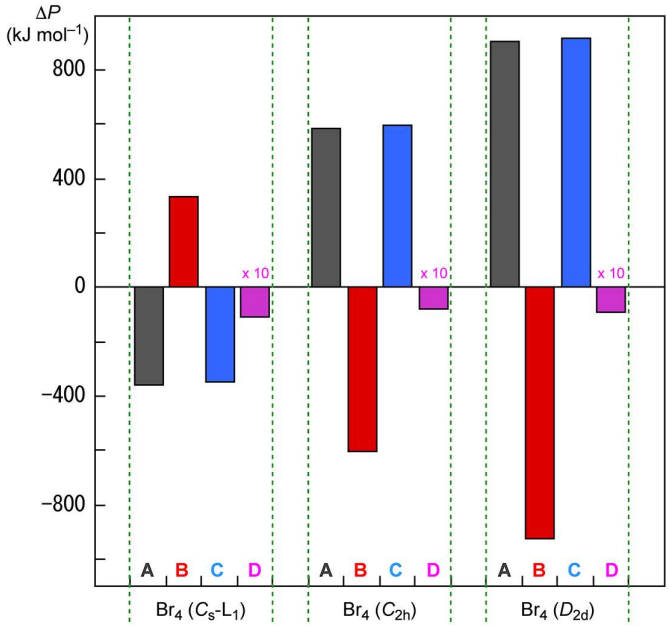

Figure 8. Contributions from $\Delta\Sigma_i^n H_c(i)$ (= ΔP = **B**) and $\Delta(\Sigma_{i\neq j}^n J_{ij} - \Sigma_{i\neq j,||}^n K_{ij})/2$ (= ΔP = **C**) to ΔE_{ES} (= ΔP = **D**, magnified by 10 times in the plot) for Br_4 (C_s-L_1), Br_4 (C_{2h}) and Br_4 (D_{2d}), relative to $2Br_2$, together with $\Delta\Sigma_{i=1}^n \varepsilon_i$ (= ΔP = **A**).

The energy profiles of Br_4 (C_{2h}) and Br_4 (D_{2d}) seem very different from that of Br_4 (C_s-L_1). The $\Delta\Sigma_{i=1}^n \varepsilon_i$ terms for Br_4 (C_{2h}) and Br_4 (D_{2d}) are evaluated to be 587.5 and 908.1 kJ mol⁻¹, respectively.

Preprints (www.preprints.org) | NOT PEER-REVIEWED | Posted: 29 April 2021 doi:10.20944/preprints202104.0768.v1

Namely, Br_4 (C_{2h}) and Br_4 (D_{2d}) would be less stable than $2Br_2$, if $\Delta\Sigma_{i=1}^{n}\varepsilon_i$ are compared. Consequently, it is difficult to explain the stability of Br_4 (C_{2h}) and Br_4 (D_{2d}), based on the MO energies. On the other hand, $\Delta\Sigma^{n} H_c(i)$ of Br_4 (C_{2h}) and Br_4 (D_{2d}) are evaluated to be –603.5 and –926.3 kJ mol^{-1}, respectively, whereas $\Delta(\Sigma_{i\neq j}^{n} J_{ij} - \sum_{i\neq j,\|}^{n} K_{ij})/2$ are 595.5 and 917.2 kJ mol^{-1}, respectively. As a result, the ($\Delta\Sigma^{n} H_c(i)$ + $\Delta(\Sigma_{i\neq j}^{n} J_{ij} - \Sigma_{i\neq j,\|}^{n} K_{ij})/2$) values are –8.0 and –9.1 kJ mol^{-1} for Br_4 (C_{2h}) and Br_4 (D_{2d}), respectively, which correspond to their ΔE_{ES} values, respectively (relative to $2E(Br_2)$). The results show that the stabilizing effect by $\Delta\Sigma^{n} H_c(i)$ overcomes the shorter electron-nuclear distances in the species in the average. The shorter electron-electron distances must destabilize Br_4 (C_{2h}) and Br_4 (D_{2d}) through the factor of $\Delta(\Sigma_{i\neq j}^{n} J_{ij} - \Sigma_{i\neq j,\|}^{n} K_{ij})/2$, which is the inverse effect form the electron-nuclear interaction on $\Delta\Sigma^{n} H_c(i)$. However, the effect of the shorter distances on $\Delta\Sigma^{n} H_c(i)$ seems to contribute more effectively than the case of $\Delta(\Sigma_{i\neq j}^{n} J_{ij} - \Sigma_{i\neq j,\|}^{n} K_{ij})/2$ in Br_4 (C_{2h}) and Br_4 (D_{2d}), although not so large.

How can the BPs in Br_4 (C_{2h}) and Br_4 (D_{2d}) be rationalized through the orbital interactions? The $\Delta\varepsilon_i$ values of Br_4 (C_{2h}) are positive for all occupied MOs, relative to the corresponding values of $2Br_2$, except for HOMO-3 (–5.5 kJ mol^{-1}), HOMO-6 (–2.9 kJ mol^{-1}), HOMO-7 (–35.8 kJ mol^{-1}) and HOMO-13 (–1.1 kJ mol^{-1}). Figure 9 illustrates the interactions to produce HOMO, HOMO-3, HOMO-4 and HOMO-7. Indeed, HOMO-7 seems well contribute to stabilize Br_4 (C_{2h}), but HOMO-4 (+40.8 kJ mol^{-1}) is also formed in the $\pi(Br_2)$–$\pi(Br_2)$ mode. Similarly, HOMO (+13.7 kJ mol^{-1}) is formed, together with HOMO-3 in the $\pi^*(Br_2)$ + $\pi^*(Br_2)$ mode. Therefore, all MOs seem not to contribute to stabilize Br_4 (C_{2h}), inherently. Nevertheless, HOMO, HOMO-4 and HOMO-7 seem to rationalize the appearance of BPs in Br_4 (C_{2h}), along the diagonal line and shorter sides of the parallelogram, although all electrons contribute to appear BPs in molecules.

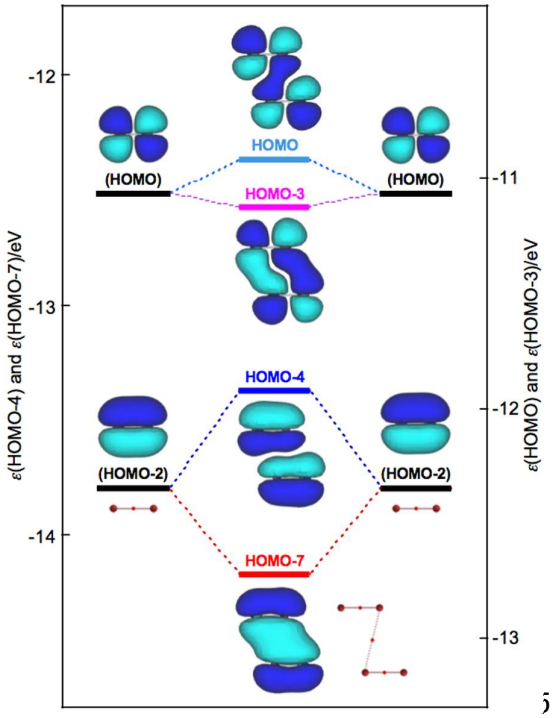

Figure 9. Energy profile for the formation of Br_4 (C_{2h}), exemplified by HOMO, HOMO-3, HOMO-4 and HOMO-7.

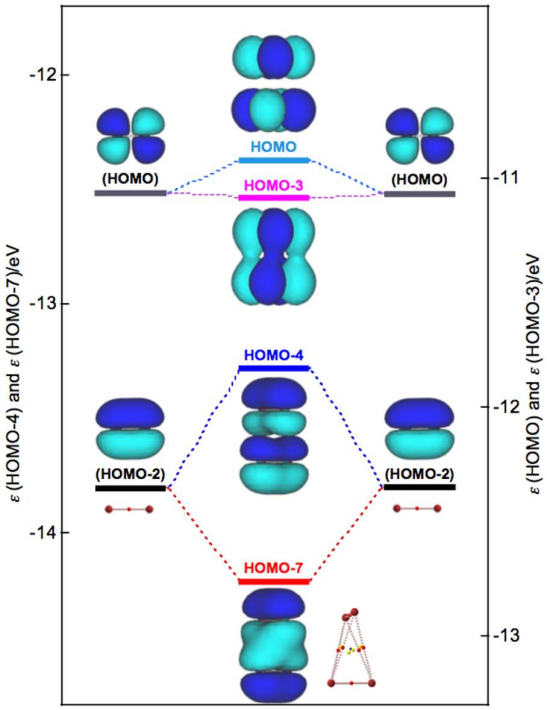

Figure 10. Energy profile for the formation of Br_4 (D_{2d}), exemplified by HOMO, HOMO-3, HOMO-4 and HOMO-7.

Similarly, $\Delta\varepsilon_i$ of Br_4 (D_{2d}) are positive for all occupied MOs, relative to the corresponding values of $2Br_2$, except for HOMO-3 (–1.9 kJ mol^{-1}), HOMO-7 (–39.2 kJ mol^{-1}) and HOMO-13 (–0.5 kJ mol^{-1}). Figure 10 illustrates the interactions to produce HOMO, HOMO-3, HOMO-4 and HOMO-7 in Br_4 (D_{2d}). HOMO-4 (+50.2 kJ mol^{-1}) is formed through the $\pi(Br_2)$–$\pi(Br_2)$ mode, in addition to HOMO-7. Similarly, HOMO (+13.9 kJ mol^{-1}) is formed, accompanied by HOMO-3 in the $\pi^*(Br_2)$ + $\pi^*(Br_2)$ mode. Therefore, no MOs essentially stabilize Br_4 (D_{2d}). However, the appearance of BPs along the longer

Preprints (www.preprints.org) | NOT PEER-REVIEWED | Posted: 29 April 2021 doi:10.20944/preprints202104.0768.v1

and shorter diagonal lines of the tetrahedron of Br_4 (D_{2d}) seem to be rationalized by HOMO-7, together with HOMO-3 and HOMO-4, modifying the BPs, although BPs will appear as the whole properties of molecules.

The nature of interactions in the charged clusters must also be of very interest. Such investigations are in progress.

4. Conclusions

The intrinsic dynamic and static nature of the non-covalent Br-∗-Br interactions was elucidated for Br_4–Br_{10} with MP2/6-311+G(3df). QTAIM-DFA was applied to the investigation. $H_b(\boldsymbol{r}_c)$ are plotted versus $H_b(\boldsymbol{r}_c) - V_b(\boldsymbol{r}_c)/2$ for the interactions at BCPs of the fully optimized structures, together with those from the perturbed structures, generated with CIV. The nature of the covalent Br-∗-Br bonds in Br_4–Br_{10} was predicted to have the SS/Cov-w nature if calculated with MP2/6-311+G(3df). On the other hands, the nature of the non-covalent Br-∗-Br interactions in Br_4–Br_{12} is classified by the *pure*-CS interactions ($\theta \le 76°$). The non-covalent Br-∗-Br interactions in the linear type clusters of Br_4 (C_s-L_1)–Br_{12} (C_s-L_5) are predicted to have the *p*-CS/*t*-HB_{nc} nature ($90.6° \le \theta_p$), except for r_2, outside ones of the first end, which have the *p*-CS/vdW nature, although it is very close to the border area between the two ($\theta_p \le 89.4°$). In the case of the cyclic clusters, the non-covalent Br-∗-Br interactions will have the *p*-CS/vdW nature ($\theta_p \le 88.4°$), except for r_2 in Br_8 (S_4) ($\theta_p = 93.5°$) and Br_8 (S_4-Wm) ($\theta_p = 95.3°$), which have the *p*-CS/*t*-HB_{nc} nature.

The energies for Br_3 σ(3c–4e) of the $n_p(Br) \rightarrow \sigma^*(Br–Br)$ type are well evaluated by not only $E(2)$ but also C_{ii}^{-1} for Br_4 (C_s-L_1)–Br_{12} (C_s-L_5). $E(2)$ correlates very well to C_{ii}^{-1}. The CT interactions of the $n_p(Br) \rightarrow \sigma^*(Br–Br)$ type must contribute to form Br_4 (C_s-L_1), which can be explained based on the MO energies, ε. However, it seems difficult to explain the stability of Br_4 (C_{2h}) and Br_4 (D_{2d}) based on the energies. The Br_2 molecules must be stacked more effectively in Br_4 (C_{2h}) and Br_4 (D_{2d}), resulting in the shorter electro-nuclear distances in the average. The energy lowering effect by $\Delta\Sigma_i^n H_c(i)$, due to the effective stacking of $2Br_2$ in Br_4 (C_{2h}) and Br_4 (D_{2d}), must contribute to form the clusters, although the inverse contribution from $\Delta((\Sigma_{i\neq j}^n J_{ij} - \Sigma_{i\neq j,||}^n K_{ij})/2)$ must also be considered.

Supplementary Materials: The following are available online at www.mdpi.com/link, Table S1: Structural parameters for Br_2–Br_6, Table S2: Structural parameters for Br_8–Br_{12}, Table S3: The bond path distances and the straight-line distances in the polybromide clusters, together with the differences between the two, Table S4: QTAIM functions and QTAIM-DFA parameters for Br-∗-Br in polybromine clusters of Br_2–Br_{12}, Table S5: Contributions from the donor-acceptor (NBO(*i*)→NBO(*j*)) interactions of the n(Br)→σ*(Br–Br) type in the optimized structures of Br_4–Br_{12} calculated with the NBO analysis, Table S6: MO energies of Br_4 (C_{2h}), Table S7: MO energies of Br_4 (D_{2d}), Table S8: MO energies of Br_2 ($D_{\infty h}$), Table S9: MO energies of Br_4 (C_s-L_1), Table S10: The $\Delta\varepsilon_i$ values for Br_4 (C_s-L_1), relative to $2Br_2$ ($D_{\infty h}$), Table S11: Energies for the Br_4 clusters and $2Br_2$, together with the differences between the two, Figure S1: Plot of ΔE_{ZP} versus ΔE_{ES} for Br_4–Br_{12}, relative to those of Br_2, respectively, Figure S2: Plots of ΔE_{ES} for Br_2–Br_{12} (C_s-L_n), Figure S3: Optimized structures for the cyclic bromine clusters of Br_8–Br_{12}, together with the linear type bromine cluster of Br_{10}, Figure S4: Plot of θ and θ_p versus R for the non-covalent Br-∗-Br interactions at the BCPs in the fully optimized structures of Br_4–Br_{12}, Figure S5: Plot of θ_p versus θ for the non-covalent Br-∗-Br interactions at the BCPs in the fully optimized structures of Br_4–Br_{12}, Figure S6: Plot of $E(2)$ versus R for the non-covalent Br-∗-Br interactions in Br_4 (C_s-L_1)–Br_{12} (C_s-L_5), Figure S7: Plot of $E(2)$ versus θ for the non-covalent Br-∗-Br interactions in Br_4 (C_s-L_1)–Br_{12} (C_s-L_5), Figure S8: Plot of $E(2)$ versus θ_p for the non-covalent Br-∗-Br interactions in Br_4 (C_s-L_1)–Br_{12} (C_s-L_5) , Figure S9: MO_i (i = 70, 67, 64, 35 and 30) and the energies relative to those corresponding to $2Br_2$, and Cartesian coordinates and energies of all the species involved in the present work. Appendix: Survey of QTAIM, closely related to QTAIM dual functional analysis, Criteria for classification of interactions: behavior of typical interactions elucidated by QTAIM-DFA, Characterization of interactions.

Acknowledgments: This work was partially supported by a Grant-in-Aid for Scientific Research (No. 26410050) from the Ministry of Education, Culture, Sports, Science and Technology of Japan. Theoretical calculations were partially performed using Research Center for Computational Science, Okazaki, Japan.

Author Contributions: S.H. and W.N. formulated the project. S.H., W.N. and T.N. optimized all compounds. T.N. and E.T. calculated the QTAIM functions and evaluated the QTAIM-DFA parameters and analyzed the data. S.H. and W.N. wrote the paper, while T.N. and E.T. organized the data to assist the writing.

Conflicts of Interest: The authors declare no conflict of interest.

References

1. Colin, J.J. Sur Quelques Combinaisons de l'Iode. *Ann. Chim.* **1814**, *91*, 252–272.
2. Cavallo, G.; Metrangolo, P.; Pilati, T.; Resnati, G.; Terraneo, G. Halogen Bond: A Long Overlooked Interaction, in Halogen Bonding I: Impact on Materials Chemistry and Life Sciences (Topics in Current Chemistry), Metrangolo, P.; Resnati, G. Eds.; Springer, New York, 2015, ch. 1, pp. 1–18.
3. Cavallo, G.; Metrangolo, P.; Milani, R.; Pilati, T.; Priimagi, A.; Resnati, G.; Terraneo, G. The Halogen Bond. *Chem. Rev.* **2016**, *116*, 2478–2601.
4. Bent, H.A. Structural chemistry of donor-acceptor interactions. *Chem. Rev.* **1968**, *68*, 587–648.
5. Desiraju, G.R.; Parthasarathy, R. The nature of halogen···halogen interactions: are short halogen contacts due to specific attractive forces or due to close packing of nonspherical atoms? *J. Am. Chem. Soc.* **1989**, *111*, 8725–8276.
6. Metrangolo, P.; Resnati, G. Halogen Bonding: A Paradigm in Supramolecular Chemistry. *Chem. Eur. J.* **2001**, *7*, 2511–2519.
7. Erdélyi, M. Halogen bonding in solution. *Chem. Soc. Rev.* **2012**, *41*, 3547–3557.
8. Beale, T.M.; Chudzinski, M.G.; Sarwar, M.G.; Taylor, M.S. Halogen bonding in solution: thermodynamics and applications. *Chem. Soc. Rev.* **2013**, *42*, 1667–1680.
9. Legon, A.C. Prereactive Complexes of Dihalogens XY with Lewis Bases B in the Gas Phase: A Systematic Case for the Halogen Analogue B···XY of the Hydrogen Bond B···HX. *Angew. Chem., Int. Ed.* **1999**, *38*, 2686–2714.
10. Politzer, P.; Murray, J.S.; Clark, T. Halogen bonding and other σ-hole interactions: a perspective. *Phys. Chem. Chem. Phys.* **2013**, *15*, 11178–11189.
11. Sugibayashi, Y.; Hayashi, S.; Nakanishi, W. Behavior of Halogen Bonds of the Y–X···π Type (X, Y=F, Cl, Br, I) in the Benzene p System, Elucidated by Using a Quantum Theory of Atoms in Molecules Dual-Functional Analysis. *Chem. Phys. Chem.* **2016**, *17*, 2579–2589.
12. Desiraju, G.R.; Ho, P.S.; Kloo, L.; Legon, A.C.; Marquardt, R.; Metrangolo, P.; Politzer, P.; Resnati, G.; Rissanen, K. Definition of the halogen bond (IUPAC Recommendations 2013). *Pure Appl. Chem.* **2013**, *85*, 1711–1713.
13. *Halogen Bonding: Fundamentals and Applications*, Metrangolo, P. Resnati, G. Eds.; Series Structure and Bonding, *Vol. 126*; Springer, 2008, New York.
14. Gierszal, K.P.; Davis, J.G.; Hands, M.D.; Wilcox, D.S.; Slipchenko, L.V.; Ben-Amotz, D. π-Hydrogen Bonding in Liquid Water. *J. Phys. Chem. Lett.* **2011**, *2*, 2930–2933.
15. The workshop entitled "*Categorizing Halogen Bonding and other Noncovalent Interactions Involving Halogen Atoms*" was organized as a satellite event of the XXII Congress and General Assembly of the International Union of Crystallography.
16. Donohue, J.; Goodman, S.H.; Interatomic distances in solid chlorine. *Acta Cryst.* **1965**, *18*, 568–569.
17. Powell, B.M.; Heal, K.M.; Torrie, B.H. The temperature dependence of the crystal structures of the solid halogens, bromine and chlorine. *Mol. Phys.* **1984**, *53*, 929.
18. Van Bolhuis, F.; Koster, P. B.; Migchelsen, T. Refinement of the crystal structure of iodine at 110° K. *Acta Cryst.* **1967**, *23*, 90–91.
19. Schuster, P.; Mikosch, H.; Bauer, All electron density functional study of neutral and ionic polybromine clusters. G. *J. Chem. Phys.* **1998**, *109*, 1833–1844.
20. See also Sung, D.; Park, N.; Park, W.; Hong, S. Formation of polybromine anions and concurrent heavy hole doping in carbon nanotubes. *Appl. Phys. Lett*. **2007**, *90*, 093502-1–093502-3.
21. Nakanishi, W.; Hayashi, S.; Narahara, K. Polar Coordinate Representation of $H_b(\boldsymbol{r}_c)$ versus $(\hbar^2/8m)\nabla^2\rho_b(\boldsymbol{r}_c)$ at BCP in AIM Analysis: Classification and Evaluation of Weak to Strong Interactions. *J. Phys. Chem. A* **2009**, *113*, 10050–10057.

22. Nakanishi, W.; Hayashi, S. Atoms-in-Molecules Dual Functional Analysis of Weak to Strong Interactions. *Curr. Org. Chem.* **2010**, *14*, 181–197.
23. Nakanishi, W.; Hayashi, S. Dynamic Behaviors of Interactions: Application of Normal Coordinates of Internal Vibrations to AIM Dual Functional Analysis. *J. Phys. Chem. A* **2010**, *114*, 7423–7430.
24. Nakanishi, W.; Hayashi, S.; Matsuiwa, K.; Kitamoto, M. Applications of Normal Coordinates of Internal Vibrations to Generate Perturbed Structures: Dynamic Behavior of Weak to Strong Interactions Elucidated by Atoms-in-Molecules Dual Functional Analysis. *Bull. Chem. Soc. Jpn*. **2012**, *85*, 1293–1305.
25. Nakanishi, W.; Hayashi, S. Role of dG/dw and dV/dw in AIM Analysis: An Approach to the Nature of Weak to Strong Interactions. *J. Phys. Chem. A* **2013**, *117*, 1795−1803.
26. Bader, R.F.W. *Atoms in Molecules. A Quantum Theory*; Oxford University Press: Oxford, UK, 1990.
27. Matta, C.F.; Boyd, R.J. An Introduction to the Quantum Theory of Atoms in Molecules In The Quantum Theory of Atoms in Molecules: From Solid State to DNA and Drug Design; WILEY-VCH: Weinheim, Germany, 2007.
28. Nakanishi, W.; Hayashi, S. Perturbed structures generated using coordinates derived from compliance constants in internal vibrations for QTAIM dual functional analysis: Intrinsic dynamic nature of interactions. *Int. J. Quantum Chem.* **2018**, *118*, e25590-1–14.
29. The basic concept for the compliance constants was introduced by Taylor and Pitzer [49], followed by Konkoli and Cremer [50].
30. The C_{ij} are defined as the partial second derivatives of the potential energy due to an external force, as shown in Equations (R1) [31–33], where i and j refer to internal coordinates, and the external force components acting on the system f_i and f_j correspond to i and j, respectively.
$$C_{ij} = \partial^2 E/\partial f_i \partial f_j \quad \text{(R1)}$$
The C_{ij} values and the coordinates corresponding to C_{ii} were calculated by using the Compliance 3.0.2 program released by Grunenberg, J. and Brandhorst, K. http://www.oc.tu-bs.de/Grunenberg/compliance.html.
31. Brandhorst, K.; Grunenberg, J. Efficient computation of compliance matrices in redundant internal coordinates from Cartesian Hessians for nonstationary points. *J. Chem. Phys.* **2010**, *132*, 184101-1–7.
32. Brandhorst, K.; Grunenberg, J. How strong is it? The interpretation of force and compliance constants as bond strength descriptors. *Chem. Soc. Rev.* **2008**, *37*, 1558–1567.
33. Grunenberg, J. III-defined concepts in chemistry: rigid force constants vs. compliance constants as bond strength descriptors for the triple bond in diboryne. *Chem. Sci.* **2015**, *6*, 4086–4088.
34. Frisch, M.J.; Trucks, G.W.; Schlegel, H.B.; Scuseria, G.E.; Robb, M.A.; Cheeseman, J.R.; Scalmani, G.; Barone, V.; Mennucci, B.; Petersson, G.A.; Nakatsuji, H.; Caricato, M.; Li, X.; Hratchian, H.P.; Izmaylov, A.F.; Bloino, J.; Zheng, G.; Sonnenberg, J.L.; Hada, M.; Ehara, M.; Toyota, K.; Fukuda, R.; Hasegawa, J.; Ishida, M.; Nakajima, T.; Honda, Y.; Kitao, O.; Nakai, H.; Vreven, T.; Montgomery Jr. J.A.; Peralta, J.E.; Ogliaro, F.; Bearpark, M.; Heyd, J.J.; Brothers, E.; Kudin, K.N.; Staroverov, V.N.; Kobayashi, R.; Normand, J.; Raghavachari, K.; Rendell, A.; Burant, J.C.; Iyengar, S.S.; Tomasi, J.; Cossi, M.; Rega, N.; Millam, J.M.; Klene, M.; Knox, J.E.; Cross, J.B.; Bakken, V.; Adamo, C.; Jaramillo, J.; Gomperts, R.; Stratmann, R.E.; Yazyev, O.; Austin, A.J.; Cammi, R.; Pomelli, C.; Ochterski, J.W.; Martin, R.L.; Morokuma, K.; Zakrzewski, V.G.; Voth, G.A.; Salvador, P.; Dannenberg, J.J.; Dapprich, S.; Daniels, A.D.; Farkas, O.; Foresman, J.B.; Ortiz, J.V.; Cioslowski, J.; Fox, D.J. *Gaussian 09* (*Revision D.01*), Gaussian, Inc., Wallingford CT, 2009.
35. Binning, R.C.; Curtiss, L.A. Compact contracted basis sets for third-row atoms: Ga–Kr. *J. Comput. Chem.* **1990**, *11*, 1206–1216.
36. Curtiss, L.A.; McGrath, M.P.; Blaudeau, J.-P.; Davis, N.E.; Binning Jr. R.C.; Radom, L. Extension of Gaussian-2 theory to molecules containing third-row atoms Ga–Kr. *J. Chem. Phys.* **1995**, *103*, 6104–6113.
37. McGrath, M.P.; Radom, L. Extension of Gaussian-1 (G1) theory to bromine-containing molecules. *J. Chem. Phys*. **1991**, *94*, 511–516.
38. Clark, T.; Chandrasekhar, J.; Spitznagel, G.W.; Schleyer, P.v.R. Efficient diffuse function-augmented basis sets for anion calculations. III. The 3-21+G basis set for first-row elements, Li–F. *J. Comput. Chem.* **1983**, *4*, 294–301.
39. Møller, C.; Plesset, M.S. Note on an Approximation Treatment for Many-Electron Systems. *Phys. Rev.* **1934**, *46*, 618–622.
40. Gauss, J. Effects of electron correlation in the calculation of nuclear magnetic resonance chemical shifts. *J. Chem. Phys.* **1993**, *99*, 3629–3643.

 doi:10.20944/preprints202104.0768.v1

41. Gauss, J. Accurate Calculation of NMR Chemical Shifts. *Ber. Bunsen-Ges. Phys. Chem.* **1995**, *99*, 1001–1008.
42. The AIM2000 program (Version 2.0) is employed to analyze and visualize atoms-in-molecules: Biegler-König, F. Calculation of atomic integration data. *J. Comput. Chem.* **2000**, *21*, 1040–1048; see also refs [26] and [27].
43. Keith, T.A. AIMAll (Version 17.11.14), TK Gristmill Software, Overland Park KS, USA, 2017, http://www.aim.tkgristmill.com.
44. The Br–Br distance in Br_2 was optimized to be 2.2806 Å with MP2/6-311+G(3df), which was very close to the observed distance in the gas phase (2.287 Å). However, the values are shorter than that determined by the X-ray crystallographic analysis (2.491 Å) by 0.210 Å. The non-covalent Br---Br distance is 3.251 Å in crystal, which is shorter than the sum of the van der Waals radii [51] by 0.45 Å.
45. The molecular graph for Br_4 (C_{2h}) was very complex and very different from that expected for it when calculated with MP2/6-311+G(3df)//MP2/6-311+G(3df). Some (ω, σ) = (3, –3) attractors appear in the molecular graph of Br_4 (C_{2h}), which do not correspond to bromine atoms. Therefore, the molecular graph for Br_4 (C_{2h}) were drawn with MP2/6-311+G(d)//MP2/6-311+G(3df), which was shown in Fig. 2. The QTAIM functions were calculated with the same method.
46. Weinhold, F.; Landis, C.R. Chemistry Education: Research and Practice in Europe **2001**, *2*, 91–104.
47. Weinhold, F.; Landis, C.R. Discovering Chemistry with Natural Bond Orbitals, Wiley, 2012.
48. Weinhold, F.; Landis, C.R. Valency and Bonding: A Natural Bond Orbital Donor-Acceptor Perspective, CUP, 2005.
49. Taylor, W.T.; Pitzer, K.S. Vibrational frequencies of semirigid molecules: a general method and values for ethylbenzene. *J. Res. Natl. Bur. Stand.* **1947**, *38*, 1–17.
50. Konkoli, Z. Cremer, D. A new way of analyzing vibrational spectra. I. Derivation of adiabatic internal modes. *Int. J. Quantum Chem.* **1998**, 67, 1–9.
51. Bondi, A. van der Waals Volumes and Radii. *J. Phys. Chem.* **1964**, *68*, 441–451.